Effect of Microstructures on the Corrosion Behavior of Reinforcing Bars (Rebar) Embedded in Concrete

Prvan Kumar Katiyar[1] · Prasanna Kumar Behera[2] · Sudhir Misra[2] · K. Mondal[1]

Abstract

This work aims at understanding the effect of microstructures (coarse, medium and fine ferrite–pearlite, martensite and tempered martensite) of a reinforced (rebar) steel developed by various heat-treatments (furnace cooling, air-cooling, force air-cooling, quenching, and tempering, respectively) on its corrosion behavior in freely aerated 3.5% NaCl + 3.5% FeCl$_3$ solution. The impressed current technique was used for forcing corrosion of the rebar, which was embedded in concrete coupon, so that correlation could be drawn between microstructure and corrosion behavior in short duration. Corrosion susceptibility increased from force air-cooled–quenched–air cooled–furnace cooled–tempered steels. The crack formation in the concrete was directly related to the rust composition and thickness, presence of crack in the rust, alpha/gamma* ratio and critical corrosion amount.

Keywords Rebar steel · Heat treatment · Microstructure · Corrosion · Concrete · Rusts

1 Introduction

Corrosion of rebar embedded in concrete is a perennial problem in reinforced concrete (RC) structures [1]. It is very well understood that the stable passive layer formed on the rebar in high pH environment maintained in the concrete becomes thermodynamically unstable either due to chloride attack or carbonation in the RC members [2]. In order to increase the service life of the RC structures, corrosion scientists and engineers primarily concentrate in developing corrosion-resistant rebar via micro-alloying. The alloy steel can serve as an effective alternative to usual plain carbon steels [1, 3]. Accordingly, high corrosion resistant rebars have been developed by using alloying elements, like Cu, Cr, and Ni, particularly for applications in coastal environments. Although these steels have been observed to possess high tensile strength and good corrosion resistance, the use of these steels is associated with the cost of alloying, which limits their utilization [4–6]. Further, it has been reported

that these high corrosion-resistant stainless steel bars are highly susceptible to pitting corrosion in chloride-containing environment [7].

The weathering steels, containing small amounts of Cu, Ni, P, and Cr, have emerged as potential substitutes for these costly steels [8, 9]. Few studies related to the weathering steels have shown that the corrosion resistance of these steels in corrosive environments is significantly better than that of the carbon steels [4, 8, 10–15]. According to Asami et al. [16], the improved corrosion resistance of the weathering steel is due to the formation of α-FeOOH, which is thermodynamically very stable rust phase. However, the contradictory results on the performance of the weathering steels have also been reported in the literature [11, 17]. As mentioned in previous studies [11, 17], the continuous immersion (either in soil or water) could lead to the formation of less protective rusts on the weathering steels than plain carbon steels. However, in the case of cyclic wet-dry conditions, rusts formed on the weathering steels have been reported to be more protective [11, 17].

Furthermore, the corrosion resistance of the weathering steel can be improved by modifying the microstructure. In this regard, Guo et al. [12] have reported that the corrosion resistance of a low carbon micro-alloyed bainitic steel is very high as compared to the conventional weathering steel in 3.5% NaCl solution. They have attributed this behavior to

✉ K. Mondal
  kallol@iitk.ac.in

1 Department of Materials Science and Engineering, Indian Institute of Technology Kanpur, Kanpur 208 016, India

2 Department of Civil Engineering, Indian Institute of Technology Kanpur, Kanpur 208 016, India

the homogeneous bainitic microstructure resulting in thinner and denser rust layer on the surface of the steel.

On the other hand, altering the microstructure of steels has always been another line of defense to protect the rebar in the concrete environment. Passivation behavior of the rebar steels can be modified by altering the microstructures and keeping the other parameters, such as environment and chemistry of rebar, fixed. This could be achieved through different heat treatment practices, which, in turn, affect the morphological distribution of various phases in the parent steels.

Salamci et al. [18] have reported that the corrosion rate of a dual-phase martensite steel increases with the martensite volume fraction in 3.5% NaCl solution. Sarkar et al. [19] have reported lower corrosion resistance of a series of dual-phase steels than the normalized ferrite–pearlite steels, due to the presence of residual stresses in the martensite in 3.5% NaCl solution. Bhagavathi et al. [20] have also compared the corrosion behavior of ferrite–martensite and ferrite–pearlite steels in 3.5% NaCl solution and observed lower corrosion rate in the case of the ferrite-martensite steel due to the formation of weaker galvanic couples in the former.

In contrast, Palacios et al. [21] have reported better corrosion resistance of a normalized steel having ferrite–pearlite microstructure than a quenched and tempered steel due to the presence of adherent passive scale of $FeCO_3$ in a CO_2 saturated NaCl solution. Osório et al. [22] have found that a normalized steel with fine ferrite–pearlite microstructure with lower interlamellar spacing exhibits the highest corrosion resistance as compared to the annealed steel with coarse ferrite–pearlite structure in 0.5 M NaCl solution. Moreover, Igwemezie et al. [23] have studied the corrosion behavior of a medium carbon steel consisting of different microstructures and reported that the normalized, annealed and oil-quenched steels have shown better performance in resisting corrosion in seawater and effluent water conditions, while the water-quenched and brine-quenched martensitic steels have shown higher corrosion rates.

The review listed herein clearly indicates that the literature on the effect of microstructures on the corrosion behavior of rebar is very limited. In fact, reported literatures on the corrosion behavior of steels having different microstructures are mainly based on electrochemical tests in different solutions, and in most of these works, the tests have been conducted on steels having different compositions [18–23]. It is worth mentioning that to the best of the knowledge of the current authors, no studies have ever been carried out on the effect of microstructures made from a single composition of steel on the corrosion response of the rebar embedded in the concrete. Hence, the present study focuses on the understanding of the corrosion behavior of rebar steels having various microstructures at a fixed composition of the steel by conducting accelerated corrosion tests when the steel is embedded in the concrete. The present work also suggests that it is the first study of this kind.

The steel rod of known composition has been subjected to five different heat treatment processes namely, furnace cooling, air cooling, forced air-cooling, water quenching, and tempering. These heat treatments lead to form mixtures of allotriomorphic ferrite grains and pearlite colonies in first two cases with different levels of fineness of the alternate lamellae of ferrite and cementite in the pearlite. In case of the forced air cooling, mixture of allotriomorphic ferrite, widmanstätten ferrite and very fine pearlite could be achieved. However, water quenching and tempering lead to form martensitic and tempered martensitic steels. Rods of these steels have been embedded in concrete to study their corrosion behavior. After that, impressed corrosion tests have been performed on the RC specimens until cracks are observed on the surface of the specimens. The time taken to initiate the crack, morphological features of the rusts formed at the interface between the concrete and the steel sample, and rust thickness, composition and related α/γ^* ratio (which is the mass ratio of {α-FeOOH/(γ-FeOOH + β-FeOOH + α-Fe$_2$O$_3$)}) have been correlated with the relative corrosion behavior of all the steels. The spectroscopic and microscopic information of the corrosion products have been analyzed in conjunction with an analytical axisymmetric plane strain model of corrosion pressure in the RC structural members in order to understand the effect of microstructures on the corrosion behavior of the rebar and failure behavior of the concrete structures. Finally, critical corrosion amount (CCA), which is the mass loss in the steel responsible for the initiation of crack in the concrete, has also been estimated using an approach reported by Behera et al. [24] and correlated to the corrosion behavior of the steels with five microstructures.

2 Experimental Procedure

2.1 Material Preparation and Heat Treatment

2.1.1 Steel

The experimental flow sheet is shown in Fig. 1. The ribbed steel rebar rod used in this study contains 0.25% C, 0.187% Si, 0.752% Mn, 0.0242% P, 0.0415% S, 0.019% Cr, 0.0227% Ni, 0.0125% Nb, 0.0487% Ta, and 98.5% Fe (all are in weight percentage) along with traces of other elements. The steel rod samples with diameter of 12 mm and a length of 30 mm were cut from the as-received rebar steel and subjected to different heat treatment practices as indicated in Table 1. Oxide scale formed on the heat-treated steels was carefully removed using a wire brush made of stainless steel. The periphery of the steel samples was later

Fig. 1 Methodology used in the present study to understand the corrosion behavior of the heat-treated steels in concrete
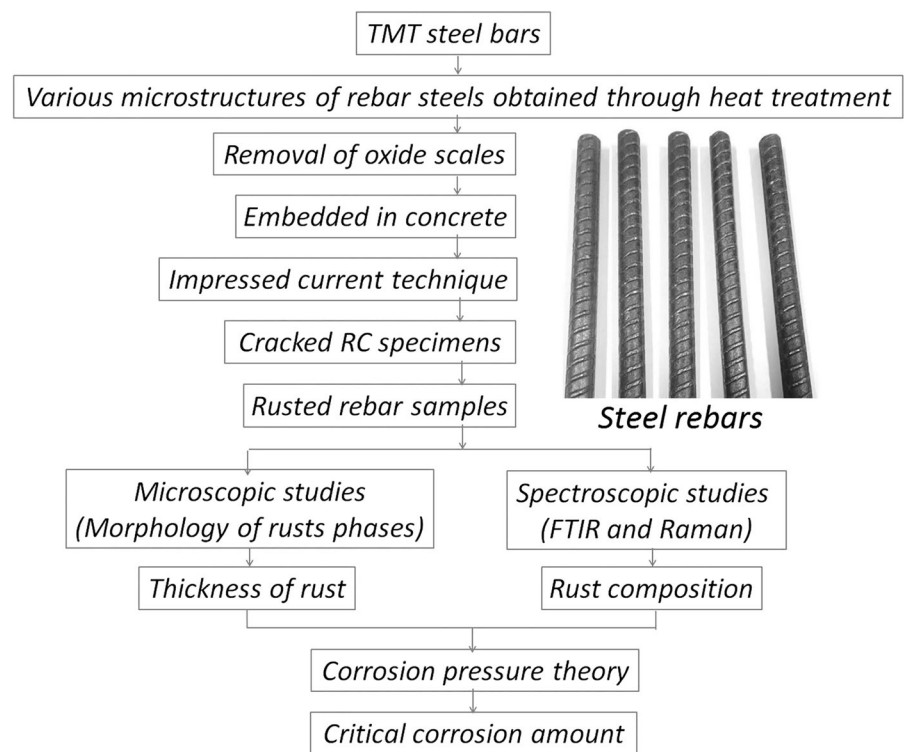
Table 1 Different heat treatments for the rebar steel and corresponding microstructure and hardness values

Materials	Process conditions	Resultant microstructure	Hardness (Vickers)
Furnace cooled	Homogenized up to 950 °C for 30 min in a muffle furnace and followed by furnace cooling (annealing)	Coarse ferrite–pearlite	165.4 ± 2.3
Air-cooled	Homogenized up to 950 °C for 30 min in a muffle furnace and followed by air cooling (normalizing)	Medium ferrite–pearlite	176.8 ± 6.7
Force air-cooled	Homogenized up to 950 °C for 30 min in a muffle furnace and cooled with the help of a table fan.	Very fine allotriomorphic ferrite and very fine pearlite with widmanstätten ferrite structure	220.4 ± 9.0
Tempered	After water quenching, steel samples again heated up to 430 °C for 4 h and followed by air cooling	Tempered martensite	326.2 ± 7.5
Quenched	Homogenized at 950 °C for 30 min in a muffle furnace and followed by water quenching.	Martensite	502.4 ± 8.8

polished using up to 1200 grit size emery paper followed by ultrasonic cleaning. This would facilitate to study the effect of microstructure exclusively, and eliminate the influence of other factors, such as surface condition and mill scale on the measurements of rust formed during corrosion testing.

For metallographic analysis, the circular sections of the samples were polished up to 2000 grit size using silicon carbide paper, followed by cloth polishing up to 0.05 μm using alumina suspension, and finally etched using 3% Nital solution. Microstructures of the heat-treated samples were examined using an optical microscope (Leica Microsystems DM6000 M) and Nova Nano SEM 450 field emission scanning electron microscope (FE-SEM). The Vicker's hardness measurement (Bareiss digi test machine) of the steel samples

was performed using a load of 100 g with a holding time of 10 s. The each reported microhardness value in the current manuscript was an average value of minimum 15 measurements taken at different locations on the steel sample.

2.1.2 Concrete

Water-cement ratio of 0.5 was maintained to prepare the concrete in this work. The commercially available chemical admixture was added to maintain the slump in a range of 70 ± 15 mm. Compressive and splitting tensile tests of concrete were performed in an universal testing machine (Instron 600 RD-E1-H2) in accordance with IS 516:1959 [25] and IS 5816:1999 [26], respectively. Compressive

strength of the concrete was obtained by testing the 150 mm cube, while the splitting tensile strength was obtained by testing the 100 mm (diameter) × 200 mm (height) concrete cylinders. The elastic modulus of the concrete was estimated in accordance with the testing procedure described in IS 516:1959 [25]. The Poisson's ratio was considered as 0.15 [27]. Details of the constituents and the properties of the concrete are given in Table 2. The tensile fracture strength of concrete (f_{cr}) was taken to be 60% of its splitting tensile strength as suggested by Hwang and Rizkalla [28].

2.2 Reinforced Concrete (RC) Specimen Preparation and Testing

RC specimens were prepared by embedding heat-treated steel rods of 12 mm diameter and 30 mm length centrally in the concrete. Dimensional details of the specimen are given in Fig. 2a. The outer diameter of the disc-shaped RC specimen was 100 mm, whereas the thickness was maintained at 30 mm. The specimens were prepared through invert mold casting. This not only facilitated proper compaction of the specimen, but also ensured that the steel was embedded exactly at the center. Therefore, it could be considered that the concrete cover thickness over the rebar was uniform (~ 44 mm) throughout the circumference of the RC specimen. It is worth mentioning that all the specimens were dipped (cured) in water for 60 days prior to testing. Since the rust thickness responsible for cracking the RC specimen was an essential parameter in the study, it is important to quantify the thickness of passive layer which usually formed on the steel surface in concrete prior to accelerated corrosion tests. Therefore, before the testing, all the RC specimens were examined in FE-SEM in order to obtain the thickness of the passive layer. However, the passive layer had not been distinguishably observed in the micrographs (data not shown), which indicated that the passive layer thickness was very low to detect. In fact, earlier researchers have also reported that the thickness of the passive layer formed on steel in concrete ranges in between 5 to 7 nm [29]. Hence, it could be understood that the thickness of the passive layer would be very low even if it had formed during the 60 days of water curing.

Accelerated corrosion tests were performed on the RC specimens by impressed current technique in freely aerated 3.5% $NaCl$ + 3.5% $FeCl_3$ solution using a DC power supply. Heat-treated steels embedded in concrete were used as anode, whereas a stainless steel 304 plate acted as a cathode. A schematic representation of testing is shown in Fig. 2b. During the experiment, a thin layer of epoxy was applied at the bottom portion of the RC specimens in order to avoid the ingress of the electrolyte from the bottom. All specimens were corroded by applying a constant voltage of 60 V throughout the testing period. It is worth mentioning that

Table 2 Details of mix constituents of the concrete

Mix proportion of constituents, kg/m³ of concrete			Chemical admixture (l/m³)	28-day compressive strength of concrete (f_c) (MPa)	Elastic modulus of concrete (E_c) (MPa)	28-day splitting tensile strength of concrete (f_t) (MPa)	Tensile fracture strength of concrete[b] (f_{cr}) (MPa)
Cement	Water	Fine aggregate	Coarse aggregate[a]				
330	165	689	1124	3.3	48.65	34,875	3.45	2.07

[a]Maximum size of coarse aggregate is 10 mm

[b]$f_{cr} = 0.6 * f_t$

Fig. 2 Schematic representation of **a** geometry of the RC specimen and **b** accelerated corrosion test set up in freely aerated 3.5% NaCl+3.5% FeCl$_3$ solution
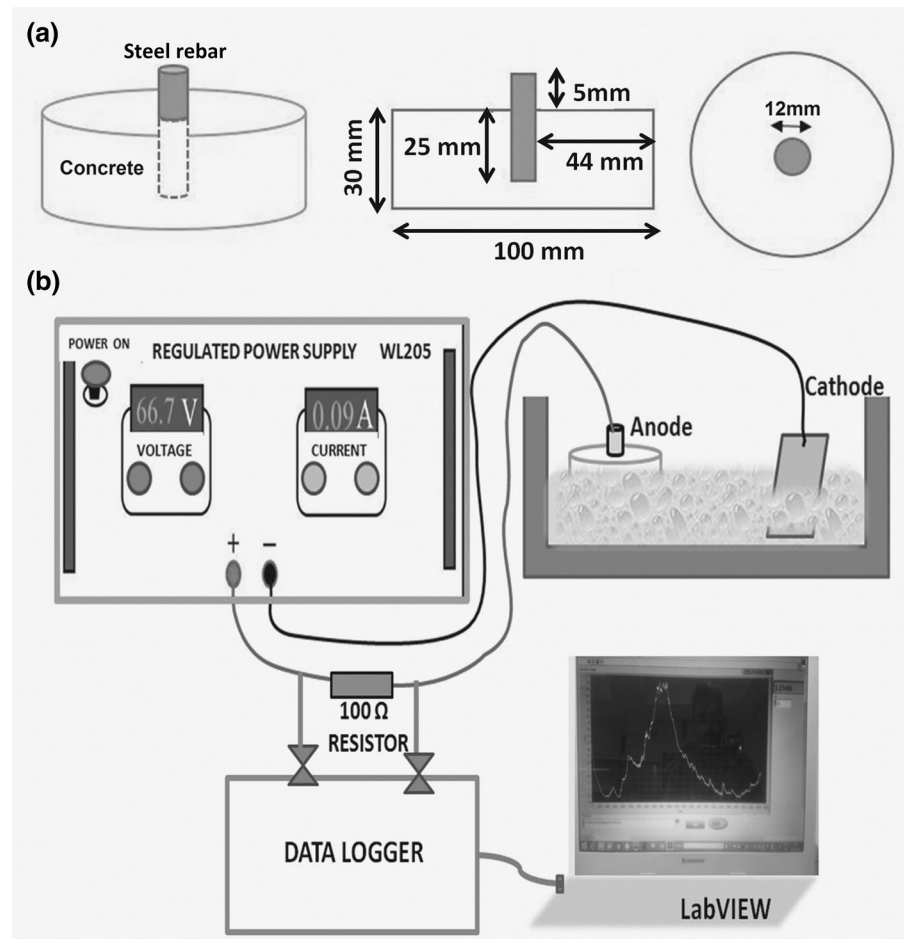
the primary focus of the present study is to initiate the crack in the specimen, and therefore applying a constant voltage would help in obtaining an idea about the time taken to initiate the crack. A 100 Ohm resistor was connected in series with the RC specimen. Current density throughout the test period was continuously recorded, which helped in capturing the event of crack initiation in the concrete.

2.3 Corrosion Product Analysis

Spectroscopic and microscopic studies of the rust samples of the cracked RC specimens were performed. The corroded steel samples (top surface as well as cross-section) from the cracked RC specimens were carefully examined with the help of a scanning electron microscope (SEM, Carl Zeiss, EVO 50) to obtain the morphology and the thickness of the rust layer at the interface between the concrete and the rebar steel. In each cracked sample, micrographs were obtained at 40 different locations along the circumference in order to calculate the rust thickness. The different features of the rust layers in the form of cracks were also observed, and an attempt to quantify the width of the crack and the fraction (%) of crack volume in rusts was made using ImageJ

software. Corrosion products or rusts were collected immediately after cracking and were examined with the help of Raman spectroscopy and Fourier transform infrared spectroscopy (FTIR) within 24 h in order to avoid the transformation of the rusts with time.

FTIR spectra of the rusts were obtained using a Bruker Tensor 27 FTIR system. For the FTIR analysis, 3 mg of rust was mixed with KBr powder to make pellets. Raman spectra of the rusts were taken on Acton Spectra Pro SP-2500 system using Nd-YAG laser of wavelength 532 nm. The relative proportions of various phases in each rust sample were calculated using Beer-Lambert's law, which states that the absorbance is equal to log (100/T), where T is the percentage of transmittance. The protective index of the rust formed after impressed current tests for all the RC samples was assessed using their α/γ^* ratio, which is the mass ratio of {α-FeOOH/(γ-FeOOH+β-FeOOH+α-Fe$_2$O$_3$)} [30–36]. The relative fractions of the rust phases obtained through relative heights of the FTIR spectrum were used in calculating α/γ^* ratio. Earlier, Behera et al. [24] and Choudhary et al. [37] have also successfully measured the relative rust fraction following the same procedure. Using the proportions of individual phases and the original amount of rust

used in FTIR analysis, the actual proportions of the phases were obtained. This information about the corrosion products was used to estimate the mass loss of iron responsible for the initiation of crack in concrete (critical corrosion amount) using the methodology described in earlier work [24].

3 Results and Discussion

3.1 Microstructure of the heat-treated steels

Microstructures pertaining to various heat treatment processes and the corresponding hardness values are listed in Table 1. Optical micrographs of the heat-treated rebar steels with five different microstructures are shown in Fig. 3a–e. Figure 3a shows typical coarse ferrite–pearlite microstructure of the furnace cooled steel, whereas, Fig. 3b shows the micrograph of the air cooled steel with fine ferrite–pearlite microstructure. Average ferrite grain size as well as the pearlite colony size of the air cooled steel have been

observed to be lower as compared to the furnace cooled steel. Values of the grain size of the ferrite phase present in the furnace cooled and air cooled of steel samples are 35.82 ± 16.86 µm and 26.62 ± 9.73 µm, respectively. The average values of the pearlite colony of the furnace cooled and the air cooled have been measured to be 30.28 ± 12.82 and 18.02 ± 6.79 µm, respectively. Figure 3c shows the optical micrograph of the force air-cooled steel, which consists of allotriomorphic ferrite, very fine pearlite and widmanstätten ferrite. Similar microstructure has been observed elsewhere [38]. The grain size of the allotriomorphic ferrite phase has been measured to be 12.22 ± 4.73 µm.

The martensite phase has been observed (Fig. 3d) as sharp needle-shaped morphology, which has been obtained by water-quenching. Tempered martensite microstructure is shown in Fig. 3e for the tempered steel, where small carbide particles are located at the plate boundaries in the needle-shaped morphology.

FE-SEM micrographs of the different microstructures of the heat-treated steels are shown in Fig. 4a–e. White colored cementite (Fe_3C) phase with different morphologies and

Fig. 3 Optical micrographs of five heat-treated rebar steels: **a** furnace cooled, **b** air cooled, **c** force air-cooled, **d** water-quenched, and **e** tempered. (F → ferrite, P → Pearlite and α → Allotriomorphic ferrite → $α_w$ → Widmanstätten ferrite)
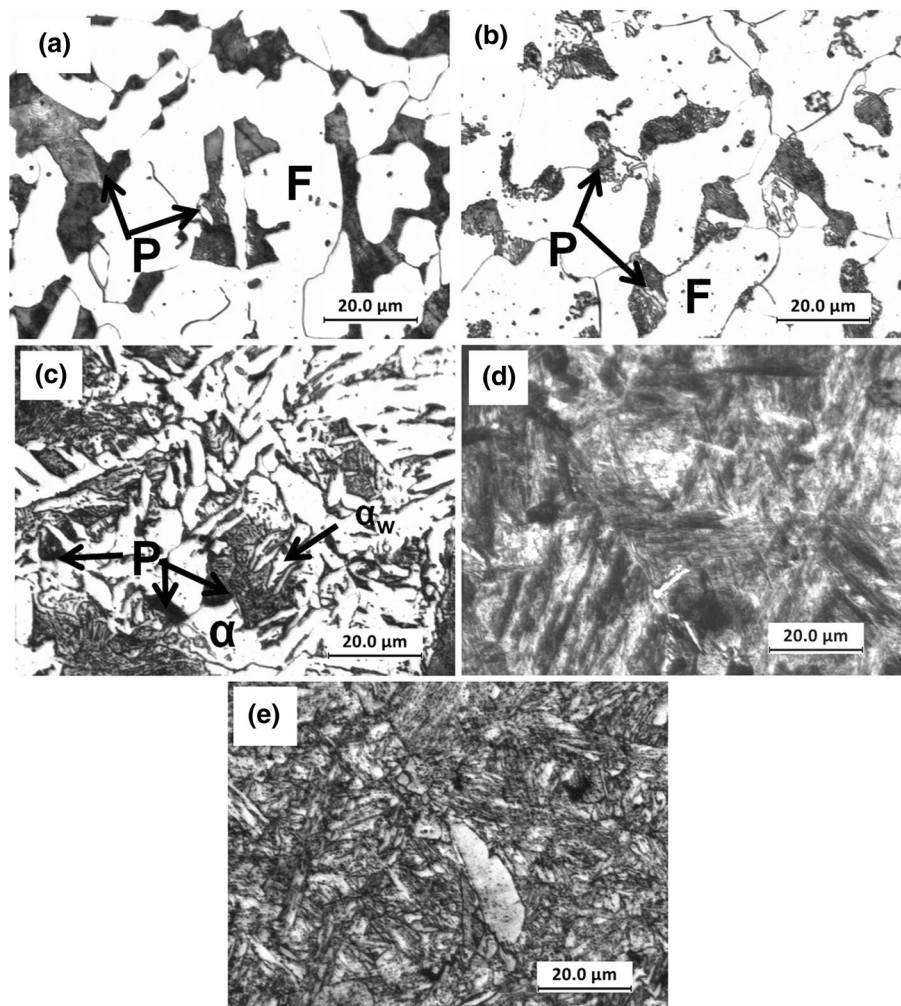
Fig. 4 FE-SEM micrographs of five heat-treated rebar steels: **a** furnace cooled, **b** air cooled, **c** force air-cooled, **d** water-quenched, and **e** tempered. Ferrite and carbide phases are in grey and white colors, respectively (F → Ferrite, C → Cementite, P → Pearlite, α → Allotriomorphic ferrite and α_w → Widmanstätten ferrite)
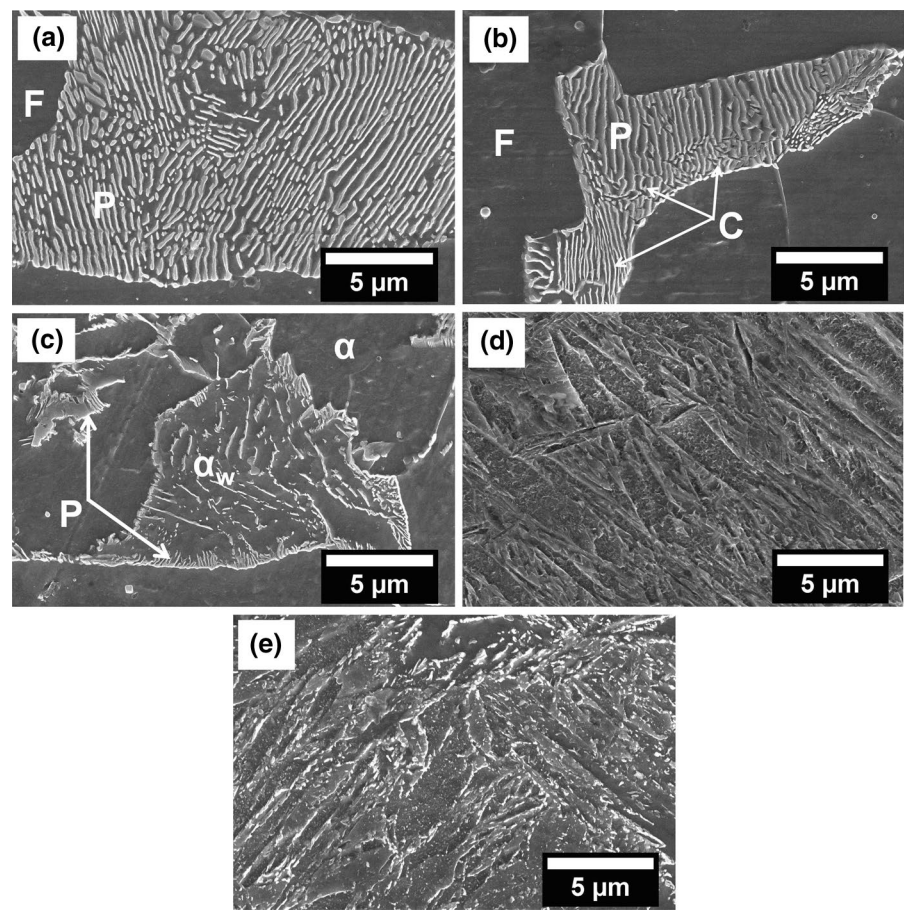
grey colored ferrite phase are clearly observed in Fig. 4a–c, e. Figure 4a, b shows the ferrite phase and alternate layer of ferrite and cementite lamellae, which is typical pearlitic microstructure. Figure 4c shows allotriomorphic ferrite, very fine pearlite and widmanstätten ferrite in the force air-cooled sample.

The values of the interlamellar spacing of the pearlitic region for the furnace cooled, air cooled, and force air cooled steels have been measured to be 0.439 ± 0.096 μm, 0.347 ± 0.091 μm, and 0.188 ± 0.074 μm, respectively. This is obtained from FE-SEM micrographs (Fig. 4a–c) using ImageJ software. The interlamellar spacing of the pearlitic regions has been found to decrease with the increase in the cooling rate from the furnace cooled to the force air-cooled steels. Martensite and tempered martensite morphologies are shown in Fig. 4d, e, respectively. Tempering of the rebar steel at 450 °C for 4 h has released the excess carbon trapped in the water-quenched martensite steel through the precipitation of carbides. The published literature has clearly shown that the martensitic finish temperature (M_f) of quenched steel having 0.25% C would be around ~250 °C [39, 40]. Since quenching was carried out in room temperature (~25 °C) in the present study, which is far less than the M_f (~250 °C), there is a very limited possibility for the

formation of retained austenite phase. Moreover, characteristic peaks of austenite have also not been observed in the XRD pattern (data not shown) of the quenched steel. Hence, there could be very low volume percentage of retained austenite even it is there, which is below the detection limit of XRD [39, 40].

The water-quenched rebar steel is the hardest, whereas, the furnace cooled ferrite–pearlite rebar steel is the softest. The hardness of the force air-cooled steel is found to be more than that of the furnace cooled and the air cooled ferrite–pearlite steels (Table 1). The resulting microstructures obtained after heat-treatment are in good agreement with the hardness values too.

3.2 Time-to-Cracking

Continuous recording of the current values has been carried out during the impressed current corrosion experiment, and the current response with time enables to capture the crack initiation and visible crack observation events in the RC specimens. In all the specimens, current densities have been found to decrease initially, because of the resistance offered by the concrete layer. At the onset of crack, a sudden increase in the current can be observed (shown
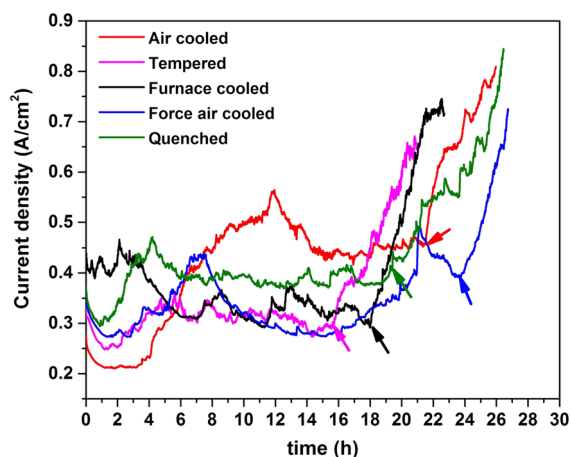
Fig. 5 Current density as a function of time during impressed current tests (arrowheads indicate the crack initiation event). The tests are stopped once visible crack has been observed and the end point also indicates the end of test

by arrowheads in Fig. 5). After this, there are steady increments in the current values for all the steels. Effectively, this attributes to the reduction in the overall resistance of the circuit due to the initiation of crack in the concrete allowing easy access of the electrolyte to the metal surface. This point of steep rise in current density is considered as the crack initiation event (Fig. 5). After the visual observation of the crack (crack observation point), the experiment has been manually stopped. The values of time taken for the crack initiation (denoted as t_{cr}), and the total time taken for visual observation of the crack (t) for the different steels are given in Table 3.

It is clearly evident that the time-to-cracking (crack observation point) largely depends on the microstructures of the steels. The cracking times (t_{cr} and t) for the RC specimen containing the tempered steel are lowest, suggesting its lowest corrosion resistance. The specimen containing the furnace cooled steel shows next better resistance to cracking as compared to that of the tempered steel. On the other hand, the force air-cooled sample shows the highest cracking

times (t_{cr} and t), indicating its highest resistance. The specimens containing the quenched and the air-cooled steels show reasonably good and nearly similar resistance to cracking. However, it is better than that of the furnace cooled steel. Thus, it is confirmed that the microstructures of the steels in the RC specimen play crucial role in governing the rate at which the specimen corrodes.

3.3 Corrosion Analysis

### 3.3.1 Rust Thickness and Morphology

Figure 6a shows the actual image of a cracked RC specimen containing the tempered steel after the corrosion test. To prepare the samples for microscopic examination, the protruded portion of the steel (as seen in Fig. 6a) has been removed from the specimens. Thereafter, the rusted steel sample has been carefully separated from the concrete. Since the RC specimen has already cracked, removing the concrete has not resulted in any major damage to the rusted steel sample. Moreover, the middle portions of the rusted steel samples have been used in the microscopic analysis. It can be considered that rusts formed after the accelerated corrosion tests are solely responsible for inducing the cracks in concrete as the thickness of the passive layer is negligible as discussed in Sect. 2.2. The schematic representation of the rust responsible for the initiation of crack in concrete is shown in Fig. 6b. As already mentioned, the scale formed after heat-treatment has been carefully removed prior to embedding them in concrete in order to study the effect of microstructure exclusively. This is confirmed through elemental mapping of the specimens (Fig. 7a). Therefore, it is very clear that the brushing of the steel surface before putting the rebar sample in the concrete has removed the scale. A typical SEM image of the corrosion products formed after the accelerated corrosion test is shown in Fig. 7b. Thickness of the rust at the middle portions of all the specimens are measured through back scattered mode (BSE) in SEM, and the presence of rust has also been confirmed through elemental mapping of Fe and O (Fig. 7b). In all the specimens, 40

Table 3 Various measurements during corrosion analysis of the cracked RC specimens of five heat treated steels

Steel embedded in concrete	Crack initiation point (t_{cr} in h)	Crack observation point (t in h)	Rust thickness (δ_r in μm)	α/γ*	Remaining diameter of the rebar (D_{ir} in mm)	Volume of rust responsible for crack in concrete (mm³/mm length of bar)	Critical corrosion amount responsible for crack in concrete (mg/cm²)
Furnace-cooled	18.3 ± 3.6	22.44 ± 1.4	105.7 ± 39.89	0.18	11.829	3.96	28.3
Air-cooled	21.4 ± 1.4	25.94 ± 1.1	112.4 ± 32.63	0.22	11.815	4.21	29.8
Forced air-cooled	23.7 ± 3.7	28.64 ± 1.5	115.5 ± 29.54	0.26	11.809	4.32	29.7
Tempered	15.7 ± 3.2	20.83 ± 3.1	99.4 ± 46.6	0.13	11.841	3.72	26.3
Quenched	20.1 ± 2.5	26.4 ± 1.39	112.9 ± 37.62	0.25	11.814	4.22	29.8

Fig. 6 a Cracked RC specimen after accelerated corrosion tests and **b** schematic representation of the rust responsible for the initiation of crack in the concrete (D_{ir}: remaining diameter of steel bar and δ_r: rust thickness)
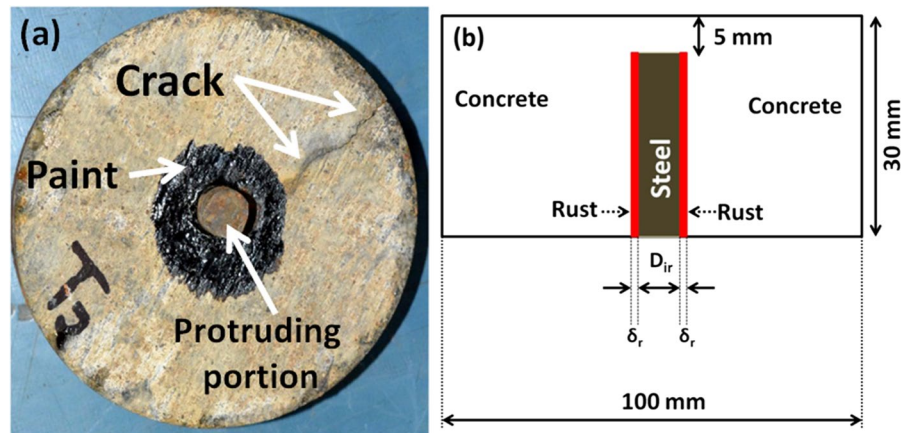
observations per sample have been taken. It should be noted that three specimens have been tested for each condition, and the average value of all the observations for a given specimen has been considered as the critical thickness of the rust responsible for the hairline crack in the concrete. The critical thicknesses are summarized in Table 3 for the various steel specimens along with the standard deviation, and the values range between 99 and 115 μm.

SEM images in BSE mode of the rust layer along the thickness direction of the cracked specimens are shown in Fig. 8. It can be seen that the rust layers formed on the steel surfaces are associated with features of cracks. Various characteristics of the rust layers are summarized in Table 4. It is clearly evident that the cracks formed along the steel-rust interface are more significant in the furnace cooled (Fig. 8a) and the tempered (Fig. 8e) steels, thereby resulting in the poor adherence of the rusts to these steels. However, the rusts formed on the air cooled (Fig. 8b), the force air-cooled (Fig. 8c) and the quenched (Fig. 8d) steels are relatively more intact, and the cracks at the interface on these steels have also been observed to be narrower than that of the furnace cooled and the tempered steels (Table 4). On the other hand, the cracks observed in the rusts of the furnace cooled and the tempered steels have been observed to be wider than those formed in the rusts of other steels. In fact, it can be clearly seen in Fig. 8a, e that the connectivity of the cracks in the rusts of the furnace cooled and the tempered steels is relatively better than the other steels. These cracks act as channel for the migration of electrolyte towards the steel through the rust layer. The crack volume in rusts (%) present in different rust layers on various steels have also confirmed the higher feasibility of dissolution of steel in the tempered and furnace cooled steels as compared to other steels.

Morphologies of the corrosion products formed on the steel samples are shown in Fig. 9. From the micrographs (Fig. 9a–j), it is clearly evident that the morphology of corrosion products formed on the surface of the rebar after corrosion test is not similar in all the steels. For instance,

the rusts formed in the furnace cooled steel have laminar worm nest morphology (Fig. 9a, f), whereas in case of the air cooled steel, the rusts mainly consist of large plate-like morphology indicating the presence of akaganeite (β-FeOOH) phase (Fig. 9b, g) [41, 42]. On the other hand, it can be seen that featureless compact rust is mainly present on the force air-cooled steel (Fig. 9c), though the magnified micrograph of Fig. 9c clearly shows the flower petals of goethite (α-FeOOH) (Fig. 9h) in the rust. In contrast, the rusts on the quenched steels predominantly have laminar bird's nest type of morphology, which indicates the presence of γ-FeOOH (Fig. 9d, i) [41, 42]. In case of the tempered steel, the porous rust associated with large plate-like morphology can be clearly seen in the micrographs (Fig. 9e, j) [41, 42]. Hence, it can be stated that microstructures of the steels greatly influence the kind of corrosion products formed in the same concrete environment.

3.3.2 Corrosion Products

FTIR and Raman spectra of the rust samples after completion of corrosion tests are shown in Fig. 10a, b, respectively. The peaks observed at the wave numbers of 1018, 869, 689 and 467 cm^{-1} correspond to γ-FeOOH, α-FeOOH, β-FeOOH and α-Fe_2O_3, respectively, in the FTIR spectra (Fig. 10a). Similarly, in the Raman spectra, α-Fe_2O_3 corresponds to the peaks at 216 and 281 cm^{-1}, and the other phases, such as peaks of α-FeOOH (385 cm^{-1}), β-FeOOH (478 cm^{-1}) and γ-FeOOH (521 and 1307 cm^{-1}) match with the reported values of these phases reported in the literature [43–45]. Thus, the identity of rust phases observed in the FTIR spectra (Fig. 10a) has been reconfirmed by the Raman spectra (Fig. 10b).

The obtained percentages of transmittance in the FTIR spectra for the various rust samples are listed in Table 5. From the spectroscopic results, it can be seen that the kinds of corrosion products present in the cracked samples are mostly similar. Though, the compositions of the rust

Fig. 7 Elemental mapping of around the interface between the steel and rust: **a** before and **b** after accelerated corrosion tests of the tempered steel (arrowhead indicates the rust)
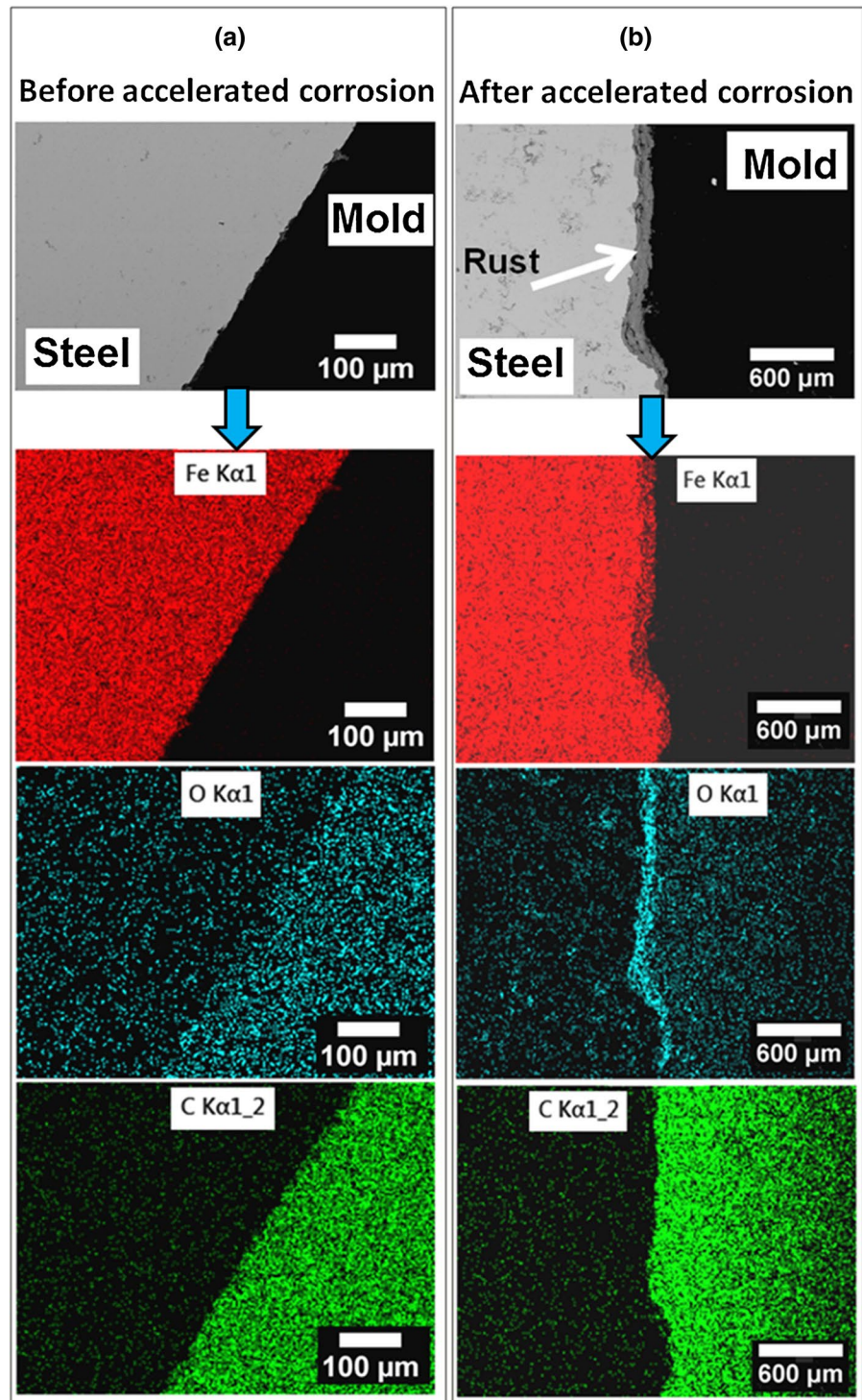

phases have significantly varied from one steel to another. Indeed, this assertion has been supported by the alpha/gamma* ratio (α/γ^*) of the rusts (Table 3). α/γ^* indicates protective ability of the rust [30–36]. Interestingly, α/γ^* of the tempered steel is the lowest indicating its lowest resistance to corrosion. This has also been confirmed by its corresponding Raman spectra, where relatively sharper and higher intensities of γ-FeOOH and β-FeOOH peaks can be observed (Fig. 10b) [46, 47].

Figure 11 shows the relationship between the time-to-cracking, percentage of crack volume in the rusts (Table 4) and the protective ability (α/γ^* ratio) of the rust phases

Fig. 8 SEM images of the interface after cracking the RC specimens embedded with various heat-treated steels: **a** furnace cooled, **b** air cooled, **c** force air-cooled, **d** quenched and **e** tempered (Solid arrow indicates the large and wide cracks while dotted arrow indicates the fine micro cracks)
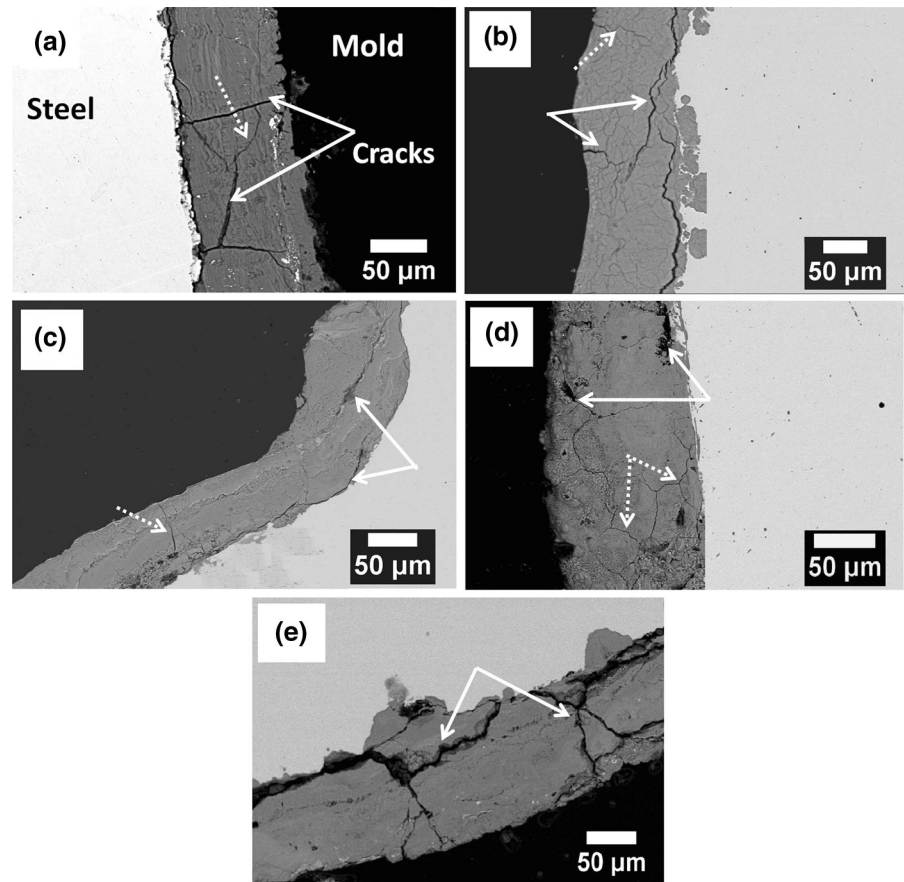

Table 4 Characteristics of the rust layers formed on five heat-treated steels

Steel	Characteristics of fissures along the steel-rust interface		Characteristics of cracks in rusts along the radial direction		Crack volume in rusts (%)
	Features of the interface	Average width of crack along the interface (μm)	Crack connectivity	Average crack width (μm)	
Furnace cooled	Less adherent	3.23 ± 1.12	High	2.05 ± 0.59	7.56 ± 1.48
Air cooled	Adherent	2.78 ± 0.94	Moderate	1.63 ± 0.67	5.98 ± 0.15
Force air-cooled	Intact and adherent	1.42 ± 0.61	Very poor	0.99 ± 0.24	3.76 ± 1.44
Quenched	Intact	3.05 ± 1.91	Limited	0.71 ± 0.151	5.52 ± 0.74
Tempered	Less adherent	9.76 ± 3.54	Very high	3.59 ± 1.20	11.19 ± 1.51

formed on the different steels. Based on the obtained results, it can be seen that the time needed to crack the concrete is inversely related to the protectiveness of the rust and the crack volume (%) present in the rust layers. The performance of the force air-cooled steel in the concrete has been found to be better than the other steels not only in terms of time-to-cracking, but also in terms of the protectiveness of the rust formed at the interface. Moreover, the rust formed on the force air-cooled steel is denser, compact and adherent in nature (Fig. 8c), and has relatively lower crack volume. This attributes to the higher cracking time in this steel. On the other hand, relatively

lower protective abilities of the rusts (low α/γ^*) have been obtained in case of the tempered and the furnace cooled steels. Accordingly, the time-to-cracking of the RC samples containing these steels has been obtained to be relatively lower. Furthermore, as mentioned above, the rusts formed on the furnace cooled steel and the tempered steel contain large numbers of wider cracks (Fig. 8a, e), which act as the channels for the migration of electrolyte towards the steel surface through the rust layer. In contrast to these steels, the rusts formed on the quenched and the air cooled steels are more protective, though, not as protective as that of the force air-cooled steel. In fact, the rusts formed

Fig. 9 Typical SEM micrographs showing the morphology of rust formed on five heat-treated steels; **a** furnace cooled, **b** air cooled, **c** force air-cooled, **d** quenched, and **e** tempered. Images **f**–**j** are the corresponding magnified images of (**a**–**e**)
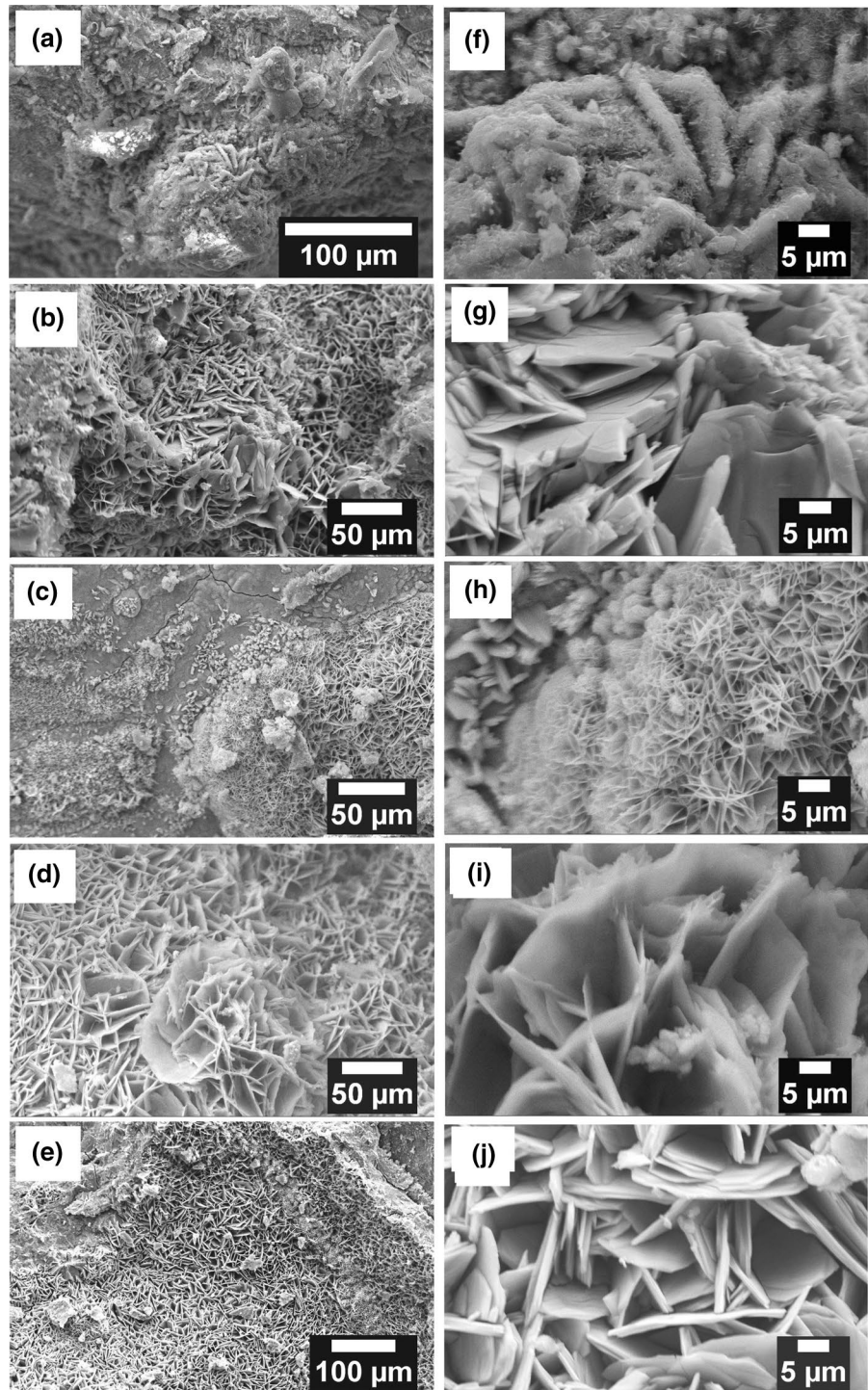
on these steels do not contain cracks to a greater extent (Fig. 8b, d). The time-to-cracking of the quenched and the air cooled steels has also been obtained to be higher than that of the furnace cooled and the tempered steels. In brief, the cracks present in the rusts of the furnace cooled and the tempered steels are wider and well interconnected, whereas, the cracks formed in the rusts formed on the quenched and the air-cooled steels are relatively narrower and less interconnected. In contrast to the rusts formed on these steels, rust layer formed on the force air-cooled steel has very less crack width and interconnected cracks.
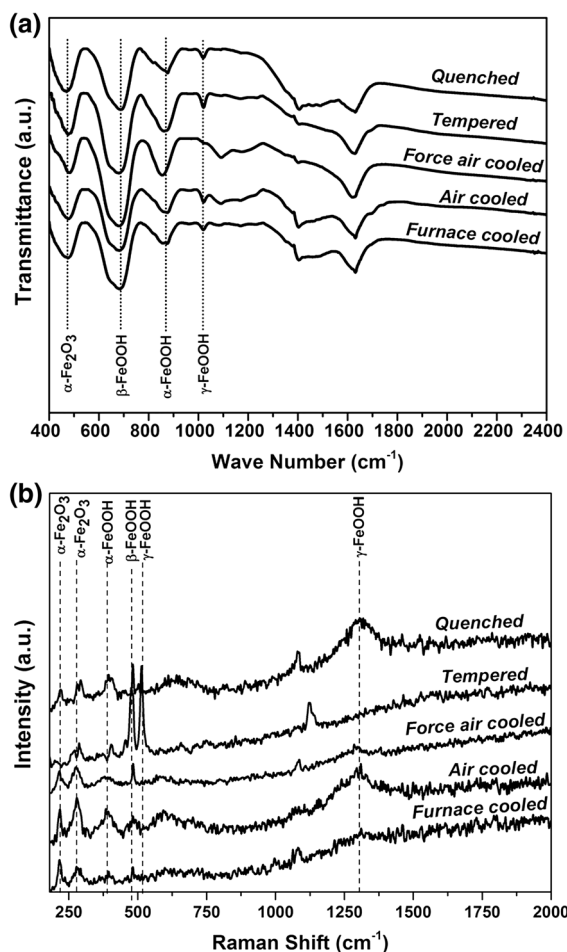
Fig. 10 a FTIR and **b** Raman spectra of the rust samples obtained from the cracked RC specimens containing five heat-treated steels

3.3.3 Relating Corrosion Pressure and Rust Products

Corrosion products formed at the interface exert pressure on the surrounding concrete. Particularly, in a study like the present one, where the impressed current technique has been used to accelerate corrosion in the rebar, the corrosion pressure on the neighbouring concrete would be uniform in nature [48, 49]. This has been modeled as a thick-walled uniform cylinder (TWUC) subjected to internal radial pressure in previously reported works (Fig. 12a) [24]. In this research, axisymmetric plane strain condition has been assumed in

order to obtain the critical pressure and corresponding displacement of the concrete at the interface. Details of the model are explained in earlier works [24, 50–53], and accordingly the critical pressure (P_c) responsible for the cracking the concrete cover is given by [24],

$$P_c = \left[\frac{E_C}{1 - \mu_c^2} \right] * \left\{ \frac{r_o^2 - r_i^2}{2r_i^2} \right\} * \varepsilon_c \tag{1}$$

where, E_c is the elastic modulus of concrete, μ_c denotes the Poisson's ratio of concrete, ε_c indicates the critical hoop strain on the surface, and r_i and r_o are the inner radius and outer radius of TWUC, respectively.

The critical hoop strain (ε_c) on the surface is related to the tensile fracture strength of concrete (f_{cr}), and it can be estimated using the following equation:

$$\varepsilon_c = f_{cr} * \left[\frac{(1 - \mu_c^2)}{E_C} \right] \tag{2}$$

The displacement of the concrete (u_{r_i}) at the surface crack initiation can be determined using the following equation:

$$u_{r_i} = \frac{P_c r_i}{E_C} \left[\left\{ \frac{r_o^2 + r_i^2}{r_o^2 - r_i^2} \right\} + \mu_c \right] \tag{3}$$

Since all the RC specimens are prepared from one particular mixture of concrete, there is no change in the properties of concrete amongst individual specimens. Therefore, the critical strain (ε_c) and the corresponding displacement of the concrete at the interface (u_{r_i}) remain same for all the RC specimens. Considering the properties of the concrete used in this study (Table 2), the critical strain at the event of surface crack initiation is calculated to be 58.1×10^{-6}. The corresponding critical pressure and the displacement of concrete at the interface are 70.84 MPa and 14.372 μm, respectively.

3.3.4 Critical Corrosion Amount

Volumetric changes at the concrete-steel interface due to the formation of rust can be visualized using a schematic representation (Fig. 12b). Two important phenomena can

Table 5 Value of FTIR transmittance peak intensities of different rust phases	Steel	Furnace cooled	Air cooled	Force air-cooled	Tempered	Quenched
	Rust phases					
	α-Fe$_2$O$_3$	89.4	90.77	79.98	84.29	75.9
	β-FeOOH	79.58	80.46	48.28	68.45	52.58
	α-FeOOH	93.64	92.48	77.66	92.20	77.89
	γ-FeOOH	98.1	96.18	98.61	92.73	92.64

Fig. 11 Correlation between the cracking time (t), protective ability and rust thickness formed on five heat-treated steels
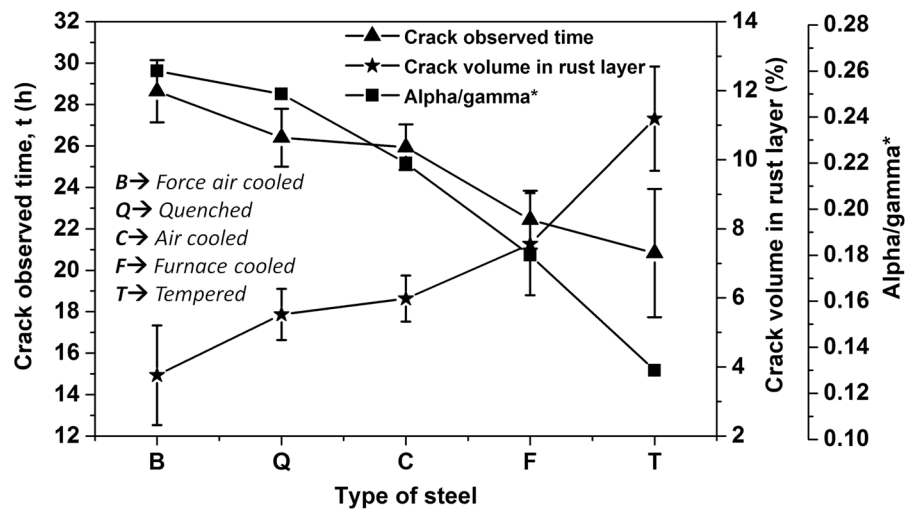
Fig. 12 a Thick-walled uniform cylinder model and **b** volumetric changes at the concrete-steel interface due to rust formation on steels (D_{is} = Initial diameter of steel; D_{ir} = remaining diameter of steel; D_{or} = Outer diameter of rust; δ_r = rust thickness; u_{ri} = radial displacement of concrete at interface)
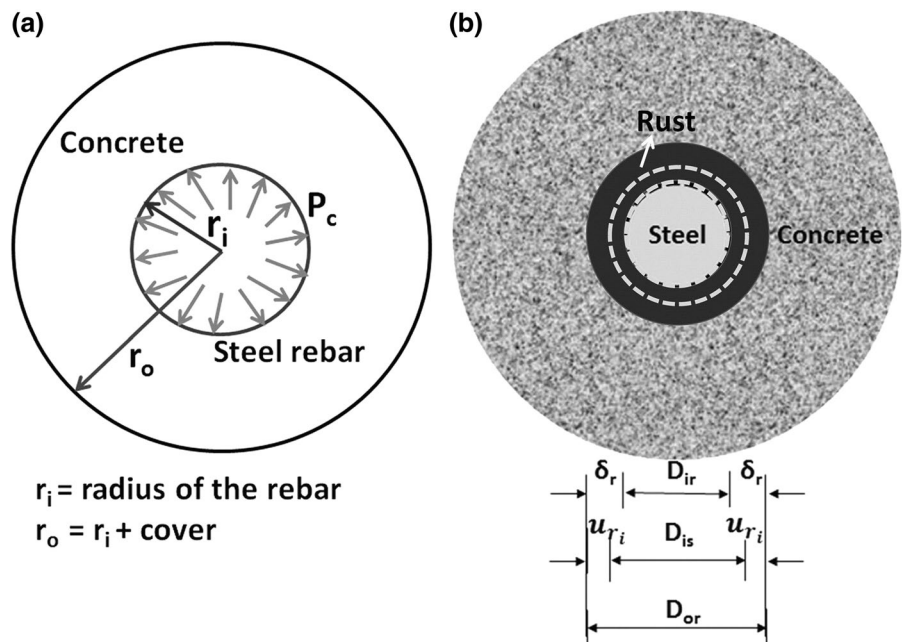
be considered for the fundamental understanding of the effect of microstructure on the reinforcement and corrosion-induced cracking in the concrete. One is the dissolution of iron at the interface, and other is the corresponding internal pressure developed by the various rust phases. Both these processes occur simultaneously, and finally result in the cracking of the concrete. The former occurs at a dynamic rate, which is dependent not only on the type of steel, but also on the kind of corrosion products formed at the interface at any given instant.

Using the procedure described in the work by Behera et al. [24], the critical extent of corrosion (CCA in mg/cm²) needed to initiate the crack in the concrete has been calculated for all the RC specimens (Table 3). The salient aspects of the approach are as follows:

- Since the cracking of the concrete is due to the expansive pressure at the interface, the critical pressure at the initiation of crack on the surface, which is only a function of properties of the concrete and geometry of TWUC, has been estimated using Eqs. (1) and (2).
- The radial displacement at the interface (u_{r_i}) due to the critical pressure has been calculated using Eq. (3).
- The volume of the rust needed to initiate the crack has been determined using the initial diameter of the rebar steel (D_{is}), radial displacement (u_{r_i}), and the thickness of the rust (δ_r) using Eqs. (4) and (5). The initial diameter (D_{is}) has been taken to be 12.012 mm (average value) for all the ribbed steels, which has been obtained by measuring the diameters of the cross-sections of the steels at approximately twenty locations taking into consideration

of the ribbed sections too. It is worth mentioning that the presence of mill scale on the steels has not been considered in the calculations, as the scales have been removed before embedding the steels in the concrete (Fig. 7a).

$$D_{or} = D_{is} + \left(2 * \left(u_{ri}\right)\right) \tag{4}$$

$$D_{ir} = D_{or} - \left(2 * \left(\delta_r\right)\right) \tag{5}$$

- The overall volume of the rust (V_r) has been proportioned (using Eq. 6) with respect to the individual rust composition, which has been further proportioned to their respective mass contributions using their densities (5.26, 3.55, 4.28 and 4.09 g/cc for α-Fe_2O_3, β-FeOOH, α-FeOOH and γ-FeOOH, respectively) reported in the literature [43].

$$V_r = \frac{\pi \left(D_{or}^2 - D_{ir}^2\right)}{4} \tag{6}$$

- Finally, the basic stoichiometric understanding has been used to back-calculate the total amount of iron lost per unit surface area (mg/cm^2) in order to cause the cracking of the RC specimen.

Results of the present study clearly indicate that the microstructures influence the composition and nature of the corrosion products. This has also reflected in the FTIR and the Raman spectra (Fig. 10a, b). Figure 13a shows the correlation between the α/γ^*, volume of the rust and critical corrosion amount (mg/cm^2) for all the steels. Few interesting inferences on the combined behavior of rust morphology and the amount of corrosion needed to cause cracking can be made from Fig. 13a. In case of the force air-cooled, the quenched and the air cooled steels, relatively higher levels of

Fig. 13 **a** Correlation between the alpha/gamma* (α/γ^*), volume of rust and critical corrosion amount formed on five heat-treated steels (the values reported are obtained from the average value of the rust thickness) and **b** schematic representation of the corrosion behavior of five heat-treated steels
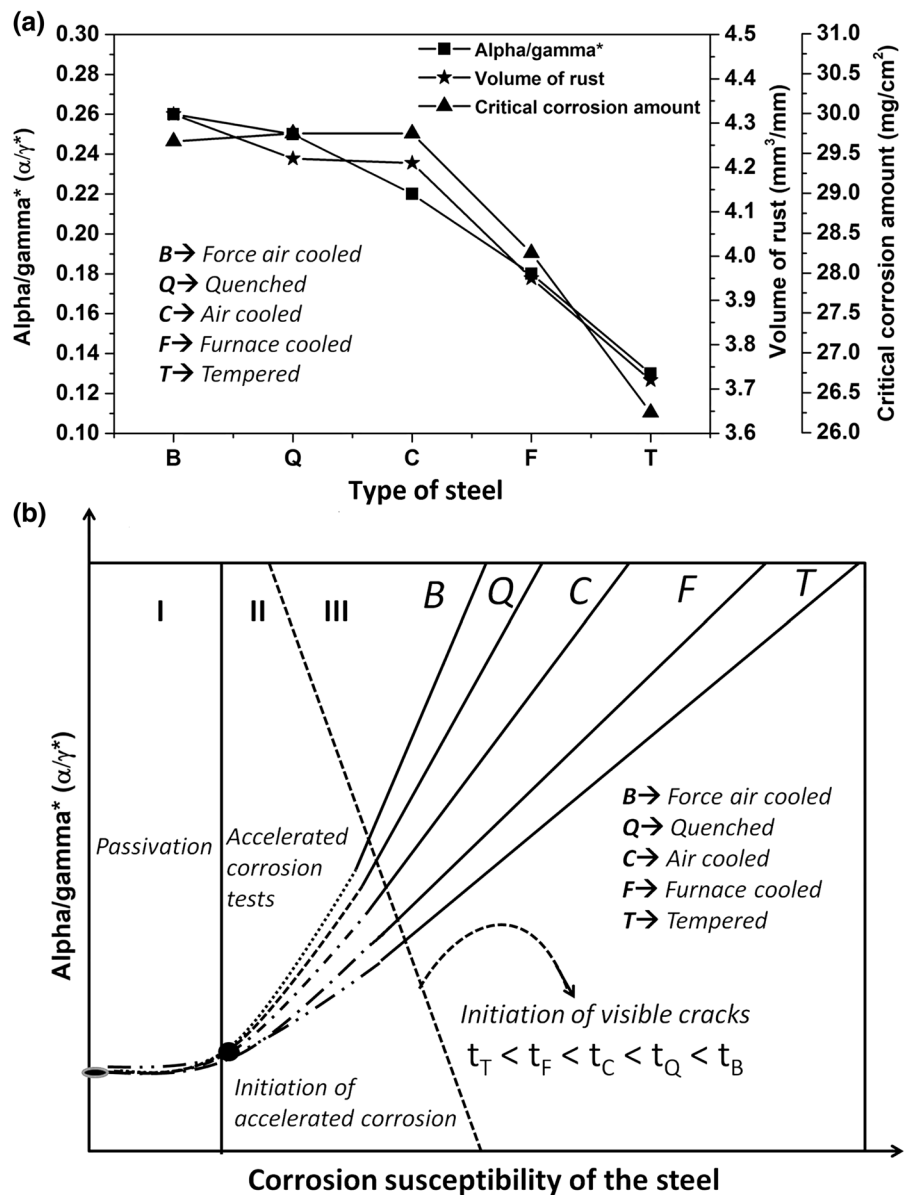
corrosion are needed to cause cracking as the rust is compact with limited cracks (Table 4). This can also be confirmed by their relatively higher α/γ* ratios. This effect has also been reflected in the form of higher cracking times in these steels (Table 3). In contrast to these steels, the critical corrosion amounts of the furnace cooled and the tempered steels are less, reflecting that the rusts in these steels are relatively porous (Figs. 8, 9).

The critical thickness, volume of the rust and the CCA have been observed to be dependent on the microstructures of the steels. Previous research related to the estimation of the CCA (either using gravimetric or non-linear FEM based approaches) have reported values in the range of 2–50 mg/cm^2 depending on the cover thickness, rebar diameter and strength of concrete [54, 55]. The estimates of CCA obtained using the spectroscopic and microscopic approaches in the present study highlighting the influence of microstructure of the rebar are in the range of 26–30 mg/cm^2, which are well within the usual range of values. It is clear from Fig. 13a that the tempered steel needs lowest rust volume as well as CCA to cause cracking in the RC specimen, and the furnace cooled steel has the next higher values. In contrast, the other three steels (force air-cooled, quenched and air cooled steels) have similar rust volumes as well as CCAs for cracking to observe, suggesting that these three steels have relatively better resistance to corrosion when embedded in concrete.

The results of the present study clearly indicate that depending on the composition of the rusts, sometimes smaller rust thicknesses are sufficient enough to cause cracking (the furnace cooled and the tempered steels). Interestingly, the rusts in the furnace cooled and the tempered steels consist of larger cracks, which would have promoted faster corrosion in the RC specimens containing these steels (Fig. 8a, e). However, the rusts in such cases are sufficiently expansive exerting the required pressure to initiate the crack in concrete. This can be interpreted from Eq. (2), according to which the critical pressure is dependent only on the properties of concrete and the geometry of the specimen used. Therefore, to exert the critical pressure on the concrete, smaller rust thicknesses need more expansive behavior to cause cracking. Thus, the thicknesses and the phases of the rusts should be considered simultaneously, and they would be such that the critical corrosion pressure would remain same in all the specimens.

The better corrosion resistance of the force air-cooled steel as compared to the air cooled and the furnace cooled steels can be attributed to the fineness of their microstructures consisting of ferrite grain, widmanstätten ferrite and pearlite. On the other hand, the better adhesiveness of the rust on the steel and relatively narrower microcracks of the force air-cooled steel could also have contributed to the better corrosion performance (Fig. 8c). Therefore, it is clear that though corrosion starts in all steels with the creation of galvanic cell between cathodic (carbide) and anodic (ferrite) phases initially, corrosion behavior after rust formation is mainly controlled by the nature of the rusts formed on the steel surface. Interestingly, similar results have been obtained elsewhere [21] based on the tests performed on the heat-treated steels in the absence of concrete, where, better corrosion performance of the fine ferrite-pearlitic steels than the martensitic and tempered steels is primarily attributed to the formation of adherent passive scale of $FeCO_3$ in a CO_2 saturated NaCl solution [21]. Rust formed on the force air-cooled steels has been observed to be more uniform and compact, which is confirmed from the results of α/γ* (Figs. 11, 8a) and morphology of the rusts (Fig. 9). Also, fine pearlite colony associated with the lower interlamellar spacing can act as a barrier to further corrosion [22, 56]. The finer microstructure would lead to more passive behavior due to the formation of stable, compact and non-porous rusts in high pH environment, like in concrete [57]. Based on the tests conducted on the heat-treated steels in 0.5 M NaCl solutions without concrete cover at 25 °C, Osório et al. [22] have also reported that higher corrosion resistance can be achieved by very fine and homogeneous distribution of pearlite colonies in the ferrite matrix in ferrite–pearlite steel.

In the present study, the corrosion susceptibility of the heat-treated steels has been evaluated on the basis of the time-to-cracking in impressed current tests and the protectiveness (α/γ*) of the rusts formed on the steels. The time-to-cracking obtained in the impressed current tests has been found to increase in the following sequence: force air-cooled–quenched–air cooled–furnace cooled–tempered steels (Fig. 5). Furthermore, the α/γ* of the rusts formed on the steels also follows the same trend (Fig. 11). Thus, the results obtained in this study has shown a fair correlation between the protectiveness (α/γ*) of the rusts formed on the steels and the corresponding time-to-cracking. In addition to the α/γ* and the time-to-cracking, various characteristics of the rusts formed on the five steels in terms of the crack present in the rusts and their connectivity have also indicated that the susceptibility of the steels to promote further dissolution decreases in the order of force air-cooled–quenched–air cooled–furnace cooled–tempered steels. Therefore, the overall corrosion performance of five heat-treated steels in the concrete can be schematically represented as shown in Fig. 13b. Finally, this study shows the influence of microstructures of five different steels made from a single composition on the corrosion behavior of rebar steels embedded in concrete for the first time along with the associated effect of the rust composition, thickness and morphology on the relative protectiveness of the RC specimens.

4 Conclusions

Corrosion behavior of the rebar steels of similar composition has been observed to be largely influenced by the steel microstructure in the concrete environment. The time taken to crack the concrete, properties of the rusts, such as presence of cracks in the rusts and their connectivity, the protective ability and the critical corrosion amount responsible for causing the crack, tend to decide the performance of the rebar steels. The rust formed on the force air-cooled steel has shown higher protectiveness (α/γ^*), lower crack volume in the rust layers and lesser interconnected cracks as compared to other steels, which have contributed for higher cracking time. Corrosion susceptibility of the steels has increased in the following sequence: force air-cooled–quenched–air cooled–furnace cooled–tempered. The sequence of corrosion susceptibility can be attributed to the different rust composition, thickness and morphology, which are again related to the typical morphologies of the developed five microstructures.

References

1. S. Ahmad, Cem. Concr. Compos. **25**, 459 (2003)
2. E.P. Kearsley, A. Joyce, J. S. Afr. Inst. Civil Eng. **56**, 21 (2014)
3. R.R. Hussain, J.K. Singh, A. Alhozaimy, A. Al-Negheimish, C. Bhattacharya, R.S. Pathania, D.D.N. Singh, ACI Mater. J. **115**, 181 (2018)
4. J. Shi, D. Ph, D. Wang, J. Ming, W. Sun, J. Mater. Civil Eng. **30**, 1 (2018)
5. M. Serdar, C. Meral, M. Kunz, D. Bjegovic, H.R. Wenk, P.J.M. Monteiro, Cem. Concr. Res. **71**, 93 (2015)
6. M. Serdar, L.V. Žulj, D. Bjegović, Corros. Sci. **69**, 149 (2013)
7. F. Presuel-Moreno, J.R. Scully, S.R. Sharp, NACE Int. Corros. Conf. Ser. **66**, 1 (2009)
8. Q.C. Zhang, J.S. Wu, J.J. Wang, W.L. Zheng, J.G. Chen, A.B. Li, Mater. Chem. Phys. **77**, 603 (2002)
9. B.K. Panigrahi, S. Srikanth, G. Sahoo, J. Mater. Eng. Perform. **18**, 1102 (2009)
10. J. Guo, S. Yang, C. Shang, Y. Wang, X. He, Corros. Sci. **51**, 242 (2008)
11. J.H. Wang, F.I. Wei, Y.S. Chang, H.C. Shih, Mater. Chem. Phys. **47**, 1 (1997)
12. J. Guo, C. Shang, S. Yang, H. Guo, X. Wang, X. He, Mater. Des. **30**, 129 (2009)
13. Q. Xu, K. Gao, W. Lv, X. Pang, Corros. Sci. **102**, 114 (2016)
14. Y.Y. Chen, H.J. Tzeng, L.I. Wei, L.H. Wang, J.C. Oung, H.C. Shih, Corros. Sci. **47**, 1001 (2005)
15. S.K. Nandi, N.K. Tewary, J.K. Saha, S.K. Ghosh, Corros. Eng. Sci. Technol. **51**, 476 (2016)
16. K. Asami, M. Kikuchi, Corros. Sci. **45**, 2671 (2003)
17. T. Misawa, K. Asami, K. Hashimoto, S. Shimodaira, Corros. Sci. **14**, 279 (1974)
18. E. Salamci, S. Candan, F. Kabakci, Kov. Mater. **55**, 133 (2017)
19. P.P. Sarkar, P. Kumar, M.K. Manna, P.C. Chakraborti, Mater. Lett. **59**, 2488 (2005)
20. L.R. Bhagavathi, G.P. Chaudhari, S.K. Nath, Mater. Des. **32**, 433 (2011)
21. C.A. Palacios, J.R. Shadley, Corrosion **47**, 122 (1991)
22. W.R. Osório, L.C. Peixoto, L.R. Garcia, A. Garcia, Mater. Corros. **60**, 804 (2009)
23. V.C. Igwemezie, J.E.O. Ovri, Int. J. Eng. Sci. **2**, 2319 (2013)
24. P.K. Behera, A. Prem, K. Moon, K. Mondal, S. Misra, J. Mater. Civil Eng. **28**, 1 (2016)
25. Indian Standard, IS 516-1959 Methods of tests for strength of concrete (2006)
26. Indian Standard, IS 5816:1999 Splitting tensile strength of concrete (1999)
27. J.M. Gere, *Mechanics of Materials*, vol. sixth (Thomson Learning Inc., Stamford, 2008)
28. L. Hwang and S. Rizkalla, in *Proceedings of the Canadian Society of Civil Engineering Structural Concrete Conference*. Natural Science and Engineering Research Council of Canada, Ottawa, ON, Canada (1983), p. 1
29. J.K. Singh, D.D.N. Singh, Corros. Sci. **56**, 129 (2012)
30. T. Nishimura, Materials **10**, 1 (2017)
31. J.T. Keiser, J. Electrochem. Soc. **129**, 2686 (1982)
32. J.T. Keiser, C.W. Brown, R.H. Heidersbach, Corros. Sci. **23**, 251 (1983)
33. I. Suzuki, J. Electrochem. Soc. **127**, 2210 (1980)
34. L. Thi, H. Lien, H.L. Hong, Mater. Sci. Appl. **4**, 6 (2013)
35. K. Asami, M. Kikuchi, J. Jpn. Inst. Metals Mater. **66**, 649 (2002)
36. Y. Waseda, S. Suzuki, *Thermodynamics for Liquid Alloys Using Electron*, vol. first (Springer, Berlin, 2006)
37. S. Choudhary, A. Garg, K. Mondal, J. Mater. Eng. Perform. **25**, 2969 (2016)
38. H.K.D.H. Bhadeshia, *Interpretation of the Microstructure of Steels* (University of Cambridge, Cambridge, 1999)
39. N. Kobasko, M. Aronov, J. Powell, J. Vanas, in *WSEAS International Conference* on *Heat Transfer, Thermal Engineering and Environment* (2009), p. 3
40. G. Kraus, *Heat Treatment and Processing Principles* (ASM International Ohio, Materials Park, 2005), pp. 63–67
41. M. Morcillo, D. De la Fuente, I. Díaz, H. Cano, Rev. Metal. **47**, 426 (2011)
42. J. Yang, Y. Lu, Z. Guo, J. Gu, C. Gu, Corros. Sci. **130**, 64 (2018)
43. R. Balasubramaniam, A.V.R. Kumar, P. Dillmann, Sci. Archaeol. Archaeomaterials **85**, 275 (2005)
44. M. Morcillo, R. Wolthuis, J. Alcántara, B. Chico, I. Díaz, D. De La Fuente, Corrosion **72**, 1044 (2016)
45. R. Balasubramaniam, A.V.R. Kumar, Corros. Sci. **42**, 2085 (2000)
46. U.M. Angst, M.R. Geiker, A. Michel, C. Gehlen, H. Wong, O.B. Isgor, B. Elsener, C.M. Hansson, R. François, K. Hornbostel, R. Polder, M.C. Alonso, M. Sanchez, M.J. Correia, M. Criado, A. Sagüés, N. Buenfeld, Mater. Struct. Constr. **50**, 1 (2017)
47. J. Alcántara, D. Fuente, B. Chico, J. Simancas, I. Díaz, M. Morcillo, Materials **10**, 1 (2017)
48. G. Malumbela, M. Alexander, P. Moyo, Constr. Build. Mater. **25**, 987 (2011)
49. T. El Maaddawy, K. Soudki, T. Topper, ACI Struct. J. **102**, 649 (2005)
50. Y. Liu, R.E. Weyers, Mater. J. **95**, 675 (1998)
51. K. Bhargava, A.K. Ghosh, Y. Mori, S. Ramanujam, Nucl. Eng. Des. **236**, 1123 (2006)
52. K. Bhargava, A.K. Ghosh, Y. Mori, S. Ramanujam, Cem. Concr. Res. **35**, 2203 (2005)
53. I. Balafas, C.J. Burgoyne, J. Eng. Mech. **137**, 175 (2011)
54. K. Suda, S. Misra, K. Motohashi, Corros. Sci. **35**, 1543 (1993)

55. K. Yokozeki, K. Motohash, K. Okada, T.T. Tsutsumi, in *Fourth CANMET/ACI International Conference* on Durability *of Concrete (SP 170-40)* (1997), p. 777

56. P.K. Katiyar, S. Misra, K. Mondal, J. Mater. Eng. Perform. **27**, 1753 (2018)

57. K.D. Ralston, N. Birbilis, Corrosion **66**, 1 (2010)